communications earth & environment

Article

A Nature Portfolio journal

https://doi.org/10.1038/s43247-026-03201-y

Self-organization of mid-ocean ridge segments during oblique oceanisation

Hao Su[1,2], Jie Liao[2,3] ✉, Sascha Brune[4,5], Taras Gerya[6] & Wei Leng[1,7] ✉

Obliquely rifted continental margins are common, yet oblique spreading ridge segments are surprisingly rare. Oblique oceanisation, as seen in the southeast Indian Ocean, the Central Gulf of Aden, and the Equatorial Atlantic, invariably evolved into orthogonal ridge segments connected by transform faults. It remains unclear why the orthogonal ridge-transform configuration is preferred, and how it develops under sustained oblique divergence. Using 3D thermomechanical numeric models, we show that slow/ultraslow oblique spreading inherited from oblique rifting is a dynamic process. It enhances asymmetric oceanic plate growth with alternating directions and spontaneously self-organizes into orthogonal ridge segments connected with transform faults. The offset and spacing of the oceanic transform faults are controlled by the obliquity angle and the spreading rate. The step-wise orthogonal ridge-transform pattern is favored because it minimizes the total length of stronger ridge segments relative to weaker transforms, thereby reducing the mechanical work required for plate separation.

Plate motions are rarely orthogonal to continental rift orientations, which frequently leads to oblique continental rifting and the formation of oblique rifted continental margins[1–3]. Previous geodynamic models tracing the evolution from continental rifting to break-up feature the development of oblique spreading ridges after oblique rifting[4–6]. In contrast, oceanic ridges in nature are predominantly characterized by an orthogonal pattern of ridge-transform faults, with oblique spreading ridges being relatively infrequent (Fig. 1a). This relation suggests a transition from oblique divergence to plate boundary segmentation during the early stages of ocean formation. Such a transition can indeed be found in the central Gulf of Aden (the region between Khanshir Al Irquah Fracture Zone and Bosaso Hami Fracture Zone), the southeast Indian Ocean, and the Equatorial Atlantic Ocean[7,8] (Fig. 1a, b), where oblique rifts evolved into small-scale orthogonal ridge segments connected by closely spaced oceanic transform faults. Notably, in all three instances, the relative plate motion and the resulting divergence obliquity during oceanisation remained constant, as evidenced by fracture zones exhibiting approximately constant orientation (Fig. 1b). As the closely spaced oceanic transform faults have no geometric correspondence onshore (Fig. 1b), it is likely that they originated after the onset of seafloor spreading[7,8]. Based on simplified 3D thermomechanical oceanic spreading models[9], it has also been suggested that after the transition from continental breakup to spreading, transform faults will grow faster from inclined ridges than from orthogonal ones. This finding can be explained through a dynamic instability that results from brittle/plastic strain weakening, which promotes asymmetric plate growth[9]. It remains, however, unclear why the resulting small-scale segmented and offset ridge-transform configuration is favored over a continuous oblique ridge and how the former evolves from the latter under a constant spreading direction[5,6,9–13].

To explore the extensional dynamics during oblique oceanisation, we conduct 3D thermomechanical numerical models that independently vary the angle of obliquity, extension velocity, temperature and strain weakening. This allows for the simulation of the complete range of oblique extension from continental rifting to seafloor spreading. Our forward models successfully reproduce the self-organization of oblique spreading ridges into an orthogonal ridge-transform system. Our results are consistent with the development of orthogonal ridge segments and oceanic transform faults observed in the Gulf of Aden, the southeast Indian Ocean, and the Equatorial Atlantic Ocean.

Results

From oblique spreading to orthogonal ridge segments

The initial model configuration (Supplementary Fig. 1), rock rheologies, and material properties are described in the "Methods" and the Supplementary

[1]State Key Laboratory of Precision Geodesy, School of Earth and Space Sciences, University of Science and Technology of China, 230026 Hefei, China. [2]School of Earth Sciences and Engineering, Sun Yat-Sen University, Southern Marine Science and Engineering Guangdong Laboratory, 519082 Zhuhai, China. [3]Guangdong Provincial Key Lab of Geodynamics and Geohazards, Zhuhai, China. [4]GFZ Helmholtz Centre for Geosciences, Potsdam, Germany. [5]Institute of Geosciences, University of Potsdam, Potsdam-Golm, Germany. [6]Institute of Geophysics, Department of Earth and Planetary Sciences, ETH Zurich, Zurich, Switzerland. [7]Mengcheng National Geophysical Observatory, University of Science and Technology of China, 233500 Mengcheng, China. ✉e-mail: liaojie5@mail.sysu.edu.cn; wleng@ustc.edu.cn

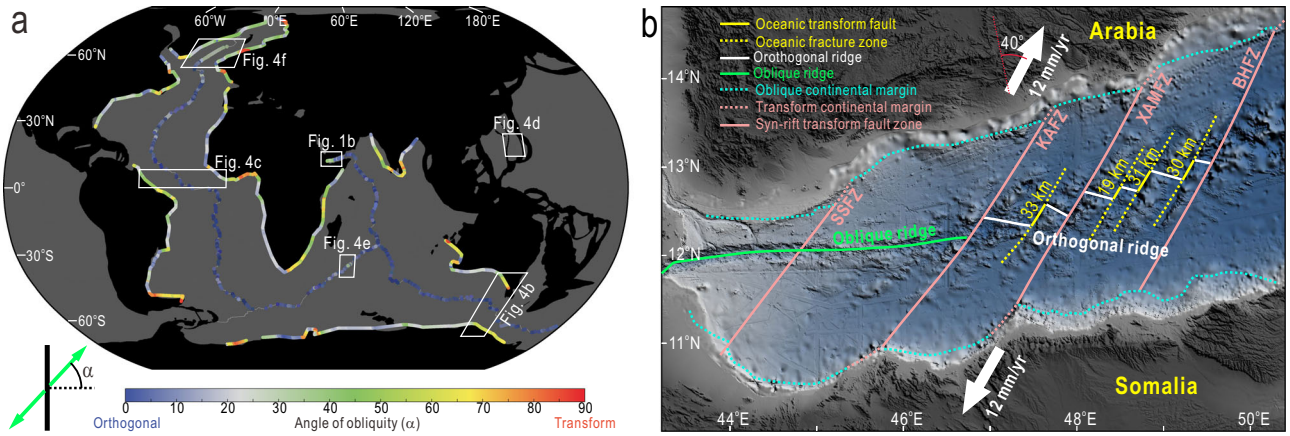

Fig. 1 | Obliquity of rifted continental margins and spreading ridges. a Global map of the obliquity of rifted continental margins and spreading ridges (based on analysis of Seton et al.[34]; Schettino et al.[45]; Demets et al.[46]). The angle of obliquity α is defined as the angle between the normal of the rift/ridge trend and the plate motion direction. **b** Simplified tectonic map of the western and central Gulf of Aden[7,8,28]. SSFZ Shukra El Sheik Fracture Zone, KAFZ Khanshir Al Irquah Fracture Zone, XAMFZ Xiis Al Mukalla Fracture Zone, BHFZ Bosaso Hami Fracture Zone.

Table 1. Figure 2 displays the oblique spreading stage of the model with an obliquity of 35° and a half extension rate of 20 mm/yr.

Once continental break-up is achieved, sea-floor spreading initiates in an oblique fashion where the mid-ocean ridge is almost straight and trends subparallel to the oblique rifted margins (Fig. 2a and Supplementary Fig. 2a). The mid-ocean ridges become curved due to asymmetric plate growth via opposite-polarity detachment faults (Figs. 2b and 3e–h; Supplementary Fig. 2b). The ridge curvature increases with time (Fig. 2c and 3i–l; Supplementary Fig. 2c). This self-organization process leads to the gradual formation of mid-ocean ridge segments. Incipient transform faults emerge that eventually cut the mid-ocean ridge into distinct segments (Fig. 2d and Supplementary Fig. 2d). The offset of the transform faults increases as the mid-ocean ridge continues to reorganize in response to asymmetric plate growth with the same polarity (Fig. 2d, e; Supplementary Fig. 2d, e). The ridge segments reorient, regulated by the transform faults, with decreasing obliquity relative to the plate motion (Fig. 2d, e). The mature transform deformation zones are characterized by large simple-shear strain rate, small pure-shear strain rate, mechanical discontinuities that cut through the entire lithosphere, spreading-parallel zones with low-relief, negligible magmatism and extremely thin oceanic crust (Figs. 2e, f and 4; Supplementary Fig. 2d–f), which are consistent with natural observations[14–19]. The transform deformation zones experience increasingly oblique shear at greater depths below the surface (Supplementary Fig. 4), consistent with a recent study showing that the transform faults are not conservative two-dimensional strike–slip plate boundaries[17].

On first order, the orthogonal ridge-transform configuration is maintained during further evolution. The spreading of the main part of ridge segments becomes approximately symmetric, while the asymmetrical spreading (detachment fault) is localized only to their ends (Fig. 2e and Supplementary Fig. 3q–v). Thus, the unstable oblique spreading ridge evolves into a stable orthogonal ridge-transform configuration during ~8 Myr (i.e., 320 km extension).

The obliquity of the spreading ridge (the angle between the normal of the spreading ridge and the plate motion) and the cumulative length of the stronger mid-ocean ridge sections decrease dramatically once the oceanic transform faults are established (Fig. 3a, b). The boundary force of oblique seafloor spreading is around 1–2 TN/m, which is comparable to the boundary force following continental break-up in a previous study[20]. At about 8 Myr, when oceanic transform faults form and the cumulative length of the mid-ocean ridge sections decrease, the boundary force required to maintain the prescribed boundary velocities decreases (Fig. 3c), and eventually stabilizes after the orthogonal ridge-transform configuration is established. These findings are independent of the obliquity, illustrated by models with various angles of obliquity showing the same trend (Figs. 2, 3 and 4a–c).

Evolution of oblique spreading ridges in various tectonic settings

We present additional models varying plate motion orientation, spreading rate and mantle potential temperature (Fig. 4 and Supplementary Figs. 5–9). The models with various angles of obliquity show a similar evolution to the reference model in terms of the formation of ridge segments and oceanic transform faults (Fig. 4a–c and Supplementary Figs. 5). Increasing the angle of obliquity leads to an increase in the offset of transform faults and a decrease in the cumulative length of the mid-ocean ridge segments, since ridge segments rotate by a larger degree to achieve orthogonal geometry. The model with orthogonal extension ($\alpha = 0°$) produces a long single ridge without oceanic transform faults due to symmetric plate growth (Fig. 4d and Supplementary Fig. 6). Varying the spreading rate of the ridge system affects the model evolution. Ultra-slow spreading favors the formation of alternating short-wave length magmatic and amagmatic segments (Supplementary Fig. 7a). The amagmatic zones favor the formation of oblique shear zones that cause the magmatic segments to become orthogonal to the spreading direction (Fig. 4e and Supplementary Fig. 7b, c). The amagmatic sections are characterized by thin oceanic crust, absence of a magma chamber, and low surface relief, but in viscosity profiles, they do not form a whole lithosphere-scale plate boundary[18] (Supplementary Fig. 7d–f). The model with higher mantle potential temperature also forms a long single ridge oblique to plate motion (Fig. 4f and Supplementary Fig. 9), because high mantle temperature enhances magma supply, which again inhibits the formation of detachment faults[21].

Discussion

Our modeling results reveal that the oblique spreading ridges inherited from oblique rifting can self-organize into a series of spreading-orthogonal ridge segments that are connected by oceanic transform faults. That transition is accommodated by asymmetric plate growth towards alternate directions governed by the detachment faults with opposite polarities[9,22]. The oceanic transform faults grow dynamically, leading to an increase in fault offsets and the re-orientation of the ridge segments. The preference of the step-wise orthogonal ridge-transform spreading patterns compared to oblique ridges is directly related to plastic strain weakening. In our models, the cohesion and effective friction coefficient linearly decrease with accumulated strain ("Methods" and Supplementary table 1). New rocks are constantly produced along the mid-ocean ridges, which do not have sufficient time to accumulate large strain. However, in the transform deformation zone, the portion of newly formed rocks is negligible, and these regions are dominated

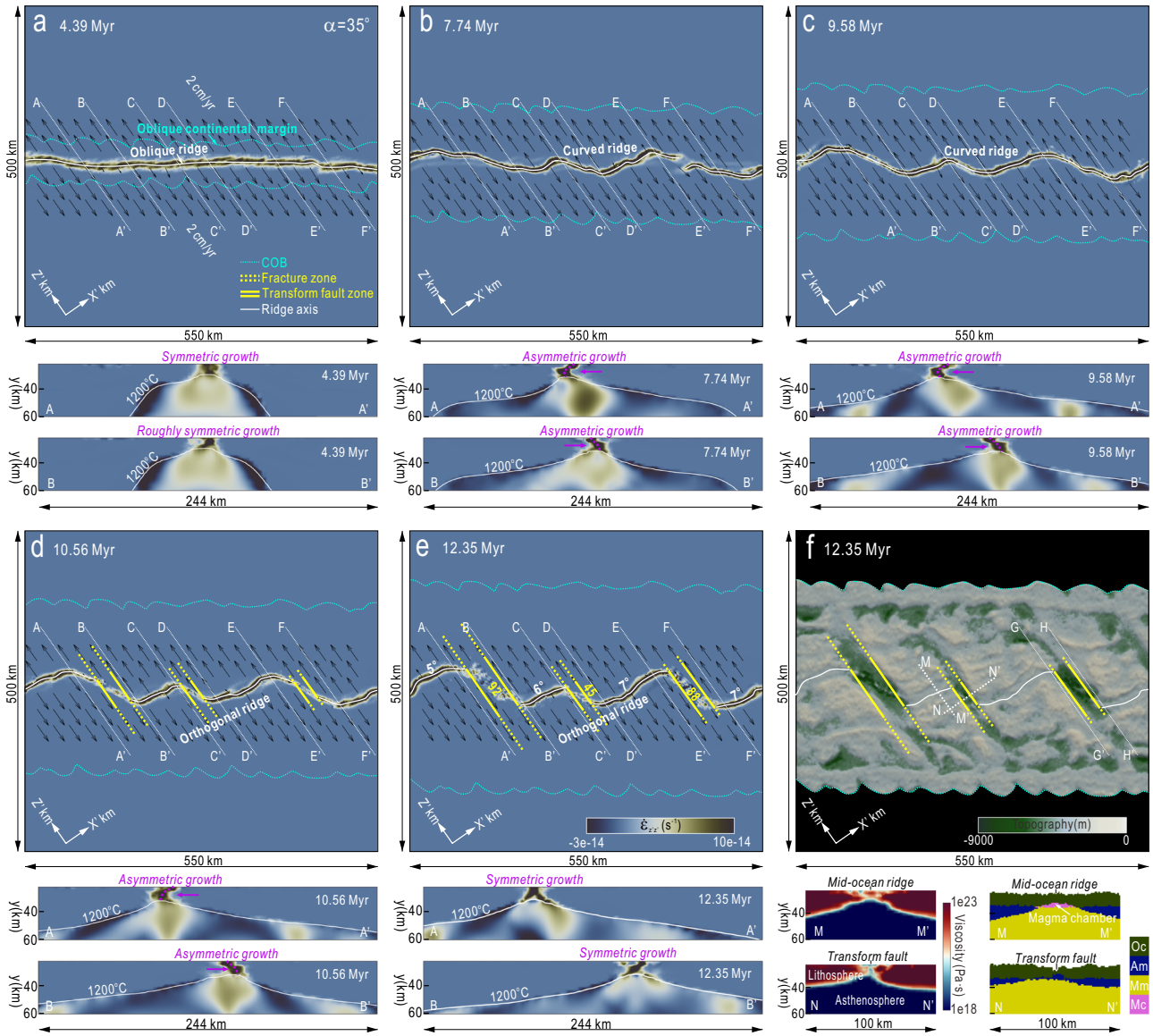

Fig. 2 | Model results showing self-organization of mid-ocean ridge segments during oblique spreading (obliquity α of 35°). a–e Snapshots of pure-shear strain rate at a depth of 2 km below seafloor and associated velocity vectors (black arrows) in a rotated x'-z' coordinate system with z' axis aligned with the imposed velocity direction at t = 4.39 Myr, 7.74 Myr, 9.58 Myr, 10.56 Myr, 12.35 Myr, respectively. The 2D strain rate profiles illustrate the styles of plate growth at mid-ocean ridge, the purple arrows indicate the movement of the mid-ocean ridge. White numbers in **e** represent the angle of obliquity of the mid-ocean ridge segments. Yellow numbers in (**e**) represent the length (in km) of transform faults. Yellow lines and yellow dotted lines depict transform faults and fracture zones, respectively. Evolution of sections C–C', D–D', E–E', F–F', G–G', H–H' are shown in Supplementary Fig. 3. **f** Snapshots of topography at t = 12.53 Myr. The sections M–M' and N–N' show the viscosity and lithology field across the mid-ocean ridge and the transform faults. COB Continent-ocean boundary, OC Oceanic crust, Am Asthenospheric mantle, Mm Molten mantle, Mc Magma chamber.

by "old" rocks that have accumulated large strain. As a consequence of strain weakening, the mid-ocean ridge sections can thus be stronger than the transform sections (Fig. 2f)[9,22,23]. Gradual mid-ocean ridge reorganization hence minimizes the cumulative length of the stronger mid-ocean ridge sections (Fig. 3b), which reduces the amount of mechanical work needed for the oblique plate divergence (Fig. 3c). We conducted a model with less plastic weakening of the oceanic lithosphere (i.e., friction coefficient reducing from 0.6 to 0.3 instead of 0.6 to 0), and model results indeed show a straight ridge without the formation of ridge/transform sections (Supplementary Fig. 9), because the formation of transforms and detachment faults is less promoted.

The offset and spacing of the oceanic transform faults are influenced by the spreading rate and the obliquity of plate motion. Model results are consistent with slow-spreading natural observations (Fig. 5). Oblique spreading in the SE Indian Ocean is affected by large obliquity[8] (~60°), which the ridge inherited from the oblique continental rift before it gradually transitioned into a state with orthogonal ridge segments that are connected by transform faults with large offsets (157 km on average, Fig. 5c and Supplementary Fig. 10c, d). In comparison, the oblique spreading ridges with smaller obliquities inherited from the continental rift that formed the Equatorial Atlantic Ocean evolved into orthogonal ridge segments bounded by transform faults with smaller offsets (82 km on average, Fig. 5c, Supplementary Fig. 10e, f). The long Romanche (over 800 km) and Chain (over 300 km) transform faults were inherited from syn-rift transform tectonics, and not from an oblique continent-ocean boundary. They formed during the formation of the continent-ocean transition[24] rather than oceanisation. Therefore, they are not included in the calculation. The spreading of the Gulf of Aden is much slower than that of the Equatorial Atlantic Ocean. During

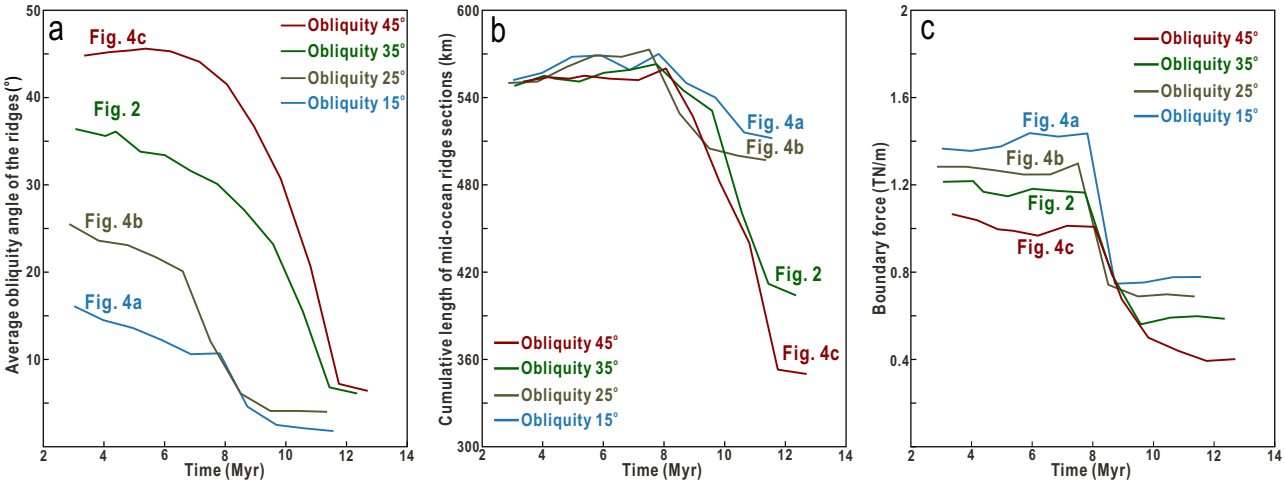

Fig. 3 | Evolution of obliquity, length of mid-ocean ridge and boundary force. **a** Average obliquity angle of the mid-ocean ridges (weighted for ridge segment length) versus time. **b** Cumulative length of the mid-ocean ridge segments versus time. **c** Boundary force versus time, the method for calculating the boundary forces is in Supplementary Information[20].

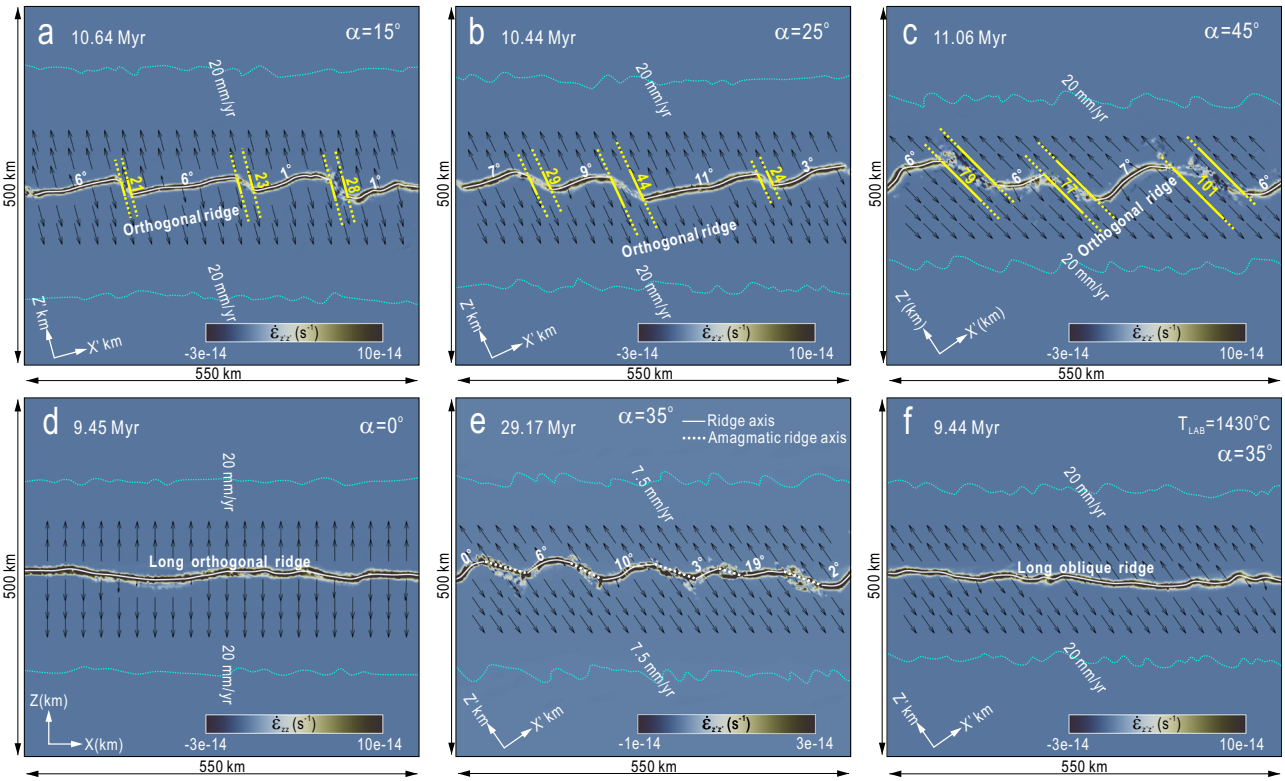

Fig. 4 | Model result in various tectonic settings showing by snapshots of pure-shear strain rate (at 2 km depth below seafloor) and associated velocity vectors. Model results with various angles of obliquity, 15° (**a**), 25° (**b**), 45° (**c**), 0° (**d**). **e** Model evolution with half extension velocity of 7.5 mm/yr. **f** Model evolution with a mantle temperature that is 50 °C higher than the reference model (Fig. 2). For detailed model evolution see Supplementary Figs. 5–9. See Fig. 2 for an explanation of numbers, lines, and arrows.

the continent-ocean transition, three long-wavelength syn-rift transform faults (KAFZ, XAMFZ, BHFZ) developed in the central Gulf of Aden[7] (Fig. 5a). The oceanic successors of these transforms divided the mid-ocean ridge into long oblique ridge segments in the early stage (Supplementary Fig. 10a). Afterwards, the long oblique ridge segments offsets gradually transitioned into short-wavelength orthogonal ridge segments and smaller lengths of transform faults (28 km on average, respectively, Fig. 5a and Supplementary Fig. 10b).

In addition to the oblique spreading inherited from oblique continental rifting as described above, another scenario forming oblique spreading is a change in the orientation of seafloor spreading. This process has been typically documented in the Parece Vela Basin of the Philippine Sea[25] (Fig. 5d). At ~22 Ma, the spreading direction in the Parece Vela Basin changed from E–W to NE–SW due to oblique subduction of the Pacific Plate[25] (Fig. 5d). Subsequently, a series of ridge segments connected by closely spaced fracture zones gradually established (Fig. 5d). This process is

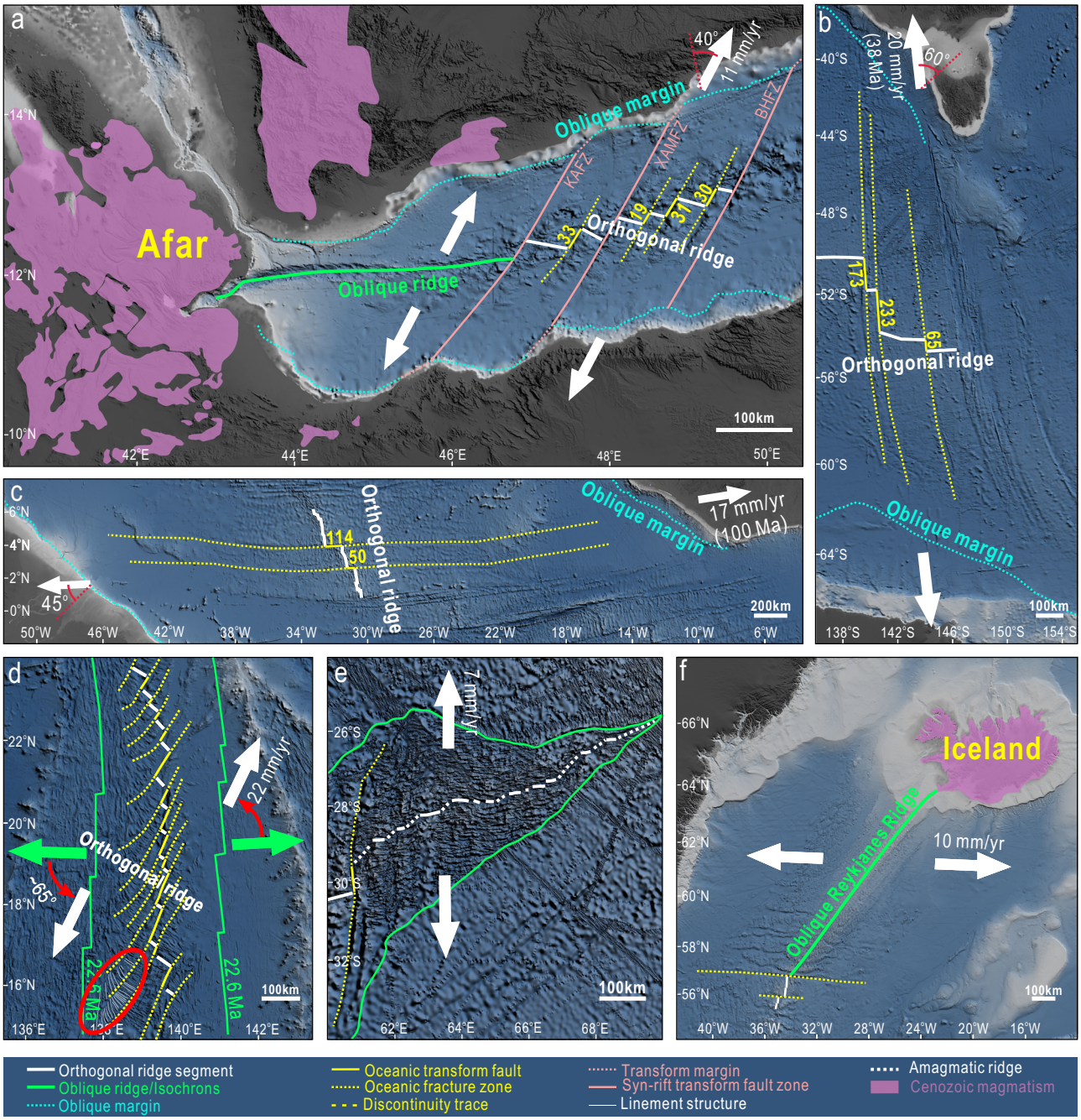

Fig. 5 | Self-organization of ridge segments in nature. Self-organization of orthogonal ridge segments during oblique oceanisation with constant plate motion in the Gulf of Aden[7,28,29] (**a**), the SE Indian ocean[8] (**b**), and the Equatorial Atlantic Ocean[8] (**c**). The yellow numbers in (**a**–**c**) represent the length (in km) of the transform faults. **d** Self-organization of orthogonal ridge segments with plate motion change in the Parece Vela Basin in the Philippine Sea[25], the dense white linear features within the red circle reflect the evolution of the mid-ocean ridge. **e** Short-wave length orthogonal magmatic sections connected by oblique amagmatic segments in the oblique ultra-slow southwest Indian Ocean[26,33]. Green arrows indicate past relative plate motions and white arrows depict current divergence direction. **f** Stabilized long single oblique ridge segments in the Reykjanes ridge[30] and in the western part of the Gulf of Aden (**a**) developed due to the influence of the Iceland and Afar plume.

well documented by the dense ridge-parallel linear structures in high-resolution bathymetry, where the long linear structures gradually break into multiple smaller segments, with their oblique angle progressively decreasing, eventually evolving into orthogonal ridge-transform fault structure (Fig. 5d). During this phase, the western part of the Parece Vela Basin experienced over 100 km of spreading, which means the ridge reorientation persisted for more than 5 Myr, which is generally consistent with our model results. The half spreading rate of the Parece Vela Basin was about 22 mm/yr at 22 Ma[8], but the spacing of fracture zones is surprisingly small (~20–55 km), which may be due to two reasons. First, a large angle of oblique spreading (~65°) generates slow effective divergence (i.e., spreading rate perpendicular to the trend of the spreading segment[26]). Second, a depleted mantle source result in small magma supply[27].

Oblique spreading ridges can be preserved as shown by our model results (Fig. 4e, f and Supplementary Fig. 9) and natural observations (Fig. 5a, e, and f). Long, single ridges maintained oblique spreading in the western Gulf of Aden and the Reykjanes Ridge (Fig. 5a, f). The preservation of these oblique plate boundaries is likely attributed to the high mantle

temperature affected by the Afar and Iceland plumes. The Afar plume affects the western Gulf of Aden, as evidenced by intense magmatism along its rifted margins and the low-velocity anomalies detected at middle mantle depths and below[28, 29] (Fig. 5a). The high mantle temperature of the Reykjanes Ridge, affected by the Iceland plume, is evidenced by the topography and the crustal thickness of the ridge axis decreases from north to south[30] (Fig. 5f). Our modeling results suggest that high mantle temperature leads to the formation of more volume of oceanic crust. As a result, mid-ocean ridges do not need detachment faults to exhume material from deeper levels to fill the gaps. Therefore, the development of detachment faults is inhibited, and thus fails to form orthogonal ridge segments during oblique spreading (Fig. 5f and Supplementary Fig. 9). Oblique ultra-slow spreading in our models favors the formation of short orthogonal magmatic sections connected by oblique amagmatic segments (Fig. 4e and Supplementary Fig. 7), which coincides with the development of oblique amagmatic sections in the ultra-slow southwest Indian (Fig. 5e), Mohns and Knipovich Ridges[31–33].

While ~70% of global rifted margins show an obliquity exceeding 20°[2,3], oblique spreading ridges are much less common than orthogonal spreading ridges[34,35] (Fig. 1a). Since the extension rate during continental rifting is commonly very low, the early seafloor spreading rates in Indo-Atlantic fall in the slow or ultraslow range, with maximum full spreading rates of no more than 50 mm/yr[36]. According to our findings, the oblique spreading ridges inherited from the oblique rift are dynamically unstable. Under slow-spreading conditions like in the Atlantic, they evolve into orthogonal spreading ridge segments connected by transform faults (Fig. 5a–c). For ultra-slow extension like in the Southwest Indian Ridge, however, oblique spreading ridges develop short orthogonal magmatic ridge segments which are connected by oblique amagmatic ridge segments[26,33] (Fig. 5e). The intermediate, fast or superfast spreading ridges in the Pacific Ocean also exhibit the orthogonal configuration[35]. But in contrast to the ridges of the Indo-Atlantic, the Pacific ridges have not been affected by plate boundary geometries inherited from continental rifting and fall outside the range of spreading rates applicable to our models.

Methods

Governing equations

We use the geodynamic code I3ELVIS, which employs finite difference and marker-in-cell methods with irregular staggered Eulerian grids to solve the continuity and momentum equations for incompressible flow and the energy equation[37,38]. The governing equations of conservation of mass, momentum and energy are:

$$\frac{\partial v_i}{\partial x_i} = 0 \tag{1}$$

$$\frac{\partial \sigma'_{ij}}{\partial x_j} - \frac{\partial P}{\partial x_i} + \rho g_i = 0 \tag{2}$$

$$\rho c_p \left(\frac{\partial T}{\partial t} + v_i \frac{\partial T}{\partial x_i}\right) = \frac{\partial}{\partial x_i}(k\frac{\partial T}{\partial x_i}) + H_r + H_s + H_a + H_L \tag{3}$$

where v_i is the velocity, σ'_{ij} is the deviatoric stress tensor, P is the pressure, ρ is the density, g_i is the gravity acceleration, c_p is the heat capacity, T is the temperature, k is the thermal conductivity, H_r, H_a, H_s and H_L are radiogenic, adiabatic, frictional, and latent heating source, respectively.

Model setup

The computational domain is 970 km (x-dimension) × 328 km (y-dimension) × 810 km (z-dimension) (Supplementary Fig. 1). The model space is resolved by 437 × 165 × 325 Eulerian nodes with uniform resolution of 2.5 × 2 × 2.5 km^3. Over 281 million Lagrangian markers are randomly distributed in the model domain to advect physical properties, such as viscosity, plastic strain and temperature. This allows for accurate tracing of rock motion.

To localize deformation, we impose a damage zone which is parallel to the x axis, 160 km wide (z = 324–484 km) and stretches down to the lithosphere-asthenosphere boundary in the model (Supplementary Fig. 1b). In this zone a random amount of initial plastic strain ranging from 0 to 0.75 is applied, the strain amplitude follows a Gaussian distribution along z axis, the location of the initial strain is random.

We impose velocity vectors oblique to the boundary to simulate oblique extension (Supplementary Fig. 1a, c). The velocities imposed on the front (z min), back (z max), left (x min) and right (z max) faces are of the same magnitude. Bounded by the middle of the z-axis, the velocity direction flips 180°. The angle of obliquity α is the angle between the velocity vector and x axis. The component of the velocity vector is computed as[39]:

$$v_x = |v| \sin\alpha \tag{4}$$

$$v_z = |v| \cos\alpha \tag{5}$$

The mass conservation of the model domain is compensated by a vertical influx v_y through the lower boundary.

$$v_{y=} \frac{2v_z \times L_x \times L_y}{L_x \times L_z} \tag{6}$$

where L_x, L_y, L_z are the length of the domain in the corresponding direction.

We also conduct an additional model with alternative boundary conditions where velocities are perpendicular to boundaries facing the x-direction and where the spreading center emerges from an oblique weak seed. We emphasize that the resulting ridge-transform-ridge pattern with 4–5 orthogonal ridge segments over a distance of ~500 km is almost identical to the one in our reference model (see the details for model setup and results in Supplementary Fig. 11).

The initial material field consists of a weak 20-km-thick sticky air layer, which allows the crustal surface to approximate a free surface[40], 15-km-thick upper crust (wet quartzite rheology), 15-km-thick lower crust (plagioclase rheology), 70-km-thick lithospheric mantle (dry olivine rheology), and the underlying 208-km-thick asthenospheric mantle (dry olivine rheology) (Supplementary Fig. 1a). Material parameter values used in the numerical experiments are listed in Supplementary Table 1.

The initial geotherm in the crust increases linearly from 0 °C at the surface to 500 °C at the Moho. The initial geotherm in the mantle lithosphere increases linearly from 500 °C at the Moho to 1380 °C at the lithosphere bottom (Supplementary Fig. 1d). We assume an adiabatic gradient of 0.5 °C km^{-1} for the subcontinental asthenospheric mantle.

Rheology

A visco-plastic rheology is applied in the entire model domain with different rheological parameters for compositionally distinct layers. Regarding the ductile rheology, the contributions from both dislocation and diffusion creeps are considered.

$$\eta_{disl} = \frac{1}{2} A^{\frac{1}{n}} \left(\dot{\varepsilon}_{\prod}\right)^{\frac{1-n}{n}} \exp\left(\frac{PV_a + E_a}{nRT}\right) \tag{7}$$

$$\eta_{diff} = \frac{1}{2} A \left(\sigma_{crit}\right)^{1-n} \exp\left(\frac{PV_a + E_a}{RT}\right) \tag{8}$$

where $\dot{\varepsilon}_{\prod}$ is the second invariant of the strain rate tensor, R gas constant, A pre-exponential factor, E_a activation energy, V_a activation volume, and n creep exponent. These values are listed in Supplementary Table 1. The effective viscosity of the viscous deformation is the harmonic average between diffusion and dislocation creep viscosity:

$$\eta_{vis} = \left(\frac{1}{\eta_{diff}} + \frac{1}{\eta_{disl}}\right) \tag{9}$$

Brittle/plastic rheology is controlled by fracture-related strain weakening[9,23,38]. It is implemented by using a Drucker-Prager criterion:

$$\eta_{plas} = \frac{\sigma_{yield}}{2\dot{\varepsilon}\prod} \tag{10}$$

$$\sigma_{yield} = C_\gamma + \varphi(P - P_f) \tag{11}$$

where η_{plas} is the effective viscosity of plastic rheology. σ_{yield} is the yield stress (Pa). P is the dynamic pressure on solids (Pa), P_f is the hydrostatic fluid pressure, C_γ is the plate strength at $P - P_f = 0$ (for both tensile and confined fracture) that depends on the plastic strain γ, defined by:

$$C_\gamma = C_0, \text{when } \gamma \le \gamma_0 \tag{12}$$

$$C_\gamma = C_0 + (\gamma - \gamma_0)\frac{C_1 - C}{\gamma_1 - \gamma_0}, \text{when } \gamma_0 < \gamma \le \gamma_1 \tag{13}$$

$$C_\gamma = C_1, \text{when } \gamma > \gamma_1 \tag{14}$$

C_0 and C_1 are the initial and final strength values for the fracture-related weakening, respectively. γ_0 and γ_1 are the upper and lower strain limits for the fracture-related weakening, respectively. φ is the internal friction coefficient, defined by:

$$\left.\begin{array}{c}\varphi = \varphi_0, \text{for} \gamma \le \gamma_0 \\ \varphi = \varphi_0 + (\gamma - \gamma_0)\frac{\varphi_1 - \varphi_0}{\gamma_1 - \gamma_0}, \text{for} \gamma_0 < \gamma \le \gamma_1 \\ \varphi = \varphi_1, \text{for} \gamma > \gamma_1\end{array}\right\}, \text{when } P \ge P_f (\text{confined fracture}) \tag{15}$$

φ_0 and φ_1 are the upper and lower limits, respectively. Strain weakening is obtained by strain-dependent linear interpolation between parameterized minimum and maximum values of φ and C_γ.

Integrated plastic strain γ (t is time and $\dot{\varepsilon}_{ij(plastic)}$ is the plastic strain rate tensor):

$$\gamma = \int \sqrt{\frac{1}{2}(\dot{\varepsilon}_{ij(plastic)})^2}dt \tag{16}$$

The effective viscosity of rocks is determined by the minimum viscosity of viscous and plastic deformation, with further limitations imposed by the cut-off values. In the case of partially molten materials (such as partially molten mantle and crustal rocks), Gerya (2013)[38] investigated the effects of constant viscosities and the dry olivine flow law on the resulting spreading patterns. In light of the aforementioned results, a constant viscosity of 10^{18} Pa s (i.e., the lower cut-off viscosity) of the partially molten materials, which is consistent with experimental petrology[41] has been incorporated into the model.

We further test a model with dry olivine rheology for the partially molten mantle where the effective viscosity of the molten mantle is about one to two orders of magnitude larger than in the reference model. We note that the resulting ridge-transform-ridge pattern is similar to the one in our reference model (see the details for model setup and results in Supplementary Fig. 12).

Magmatism

In order to model plate break-up and oceanic spreading, magma-related processes (melt generation, extraction, percolation and accretion) are implemented in our models in a simplified manner as described by Gerya[38]. The segmented nature of mantle melting at slow/ultraslow mid-ocean ridges may lead to a corresponding chemical and rheologic segmentation of the residual mantle, which probably play a role in the formation of transform faults[42,43]. We do not currently incorporate this process. The melt fraction (M) of the dry mantle is based on the parameterized melting model from Katz et al.[44]:

$$M = \begin{cases} 0 & \text{for} T \le T_s \\ \frac{T - T_s}{T_l - T_s} & \text{for} T_s < T < T_l \\ 1 & \text{for} T \ge T_l \end{cases} \tag{17}$$

where T_s, T_l are the mantle solidus, mantle liquidus, respectively.

Partial melting occurs in a wide area similar to the melt pooling region[15], and melt is extracted and stored in the shallowest part of the partial melting area. Lagrangian markers track the amount of melt extracted during model evolution. At each time step, a certain amount of melt is extracted based on the following formulation:

$$\delta M = M - \sum_{i=1}^{n} M_i^{\text{ext}} \tag{18}$$

where n is the previous extraction episodes, and M_i^{ext} is the extracted melt at each time step. The rock is considered non-molten when the extracted melt fraction is larger than the standard melt fraction ($\delta M < 0$). Extracted mantle melts first travel vertically until they reach the mantle solidus surface under the lithosphere and then migrate along this surface toward regions with the highest local surface topography, where they form a crustal magma chamber. To ensure melt volume conservation and account for mantle compaction and subsidence in response to the melt extraction, melt addition to the bottom of the magma region is performed at every time step by converting shallowest markers of hot partially molten mantle into magma markers. At each time step, the volume of converted markers matches that of extracted assembled melts computed for the time step. As a result of this treatment, partially molten mantle always contains a small amount (<1 vol %) of melt as this melt is continuously extracted and added to crustal magma chambers. The extracted melt at the next time step will be added to the bottom of the magma chamber.

Spontaneous cooling and crystallization of melts are implemented at the walls of the lower-crustal magma chambers, by simply converting the rock type from molten to solid[38]. This simple process does not account for volcanic and diking processes above the magma regions. Rapid cooling of newly formed oceanic crust is implemented through a simplified temperature and depth-dependent hydrothermal circulation approach[22,38].

Data availability

The modeling data generated in this study have been deposited in the Zenodo repository (https://doi.org/10.5281/zenodo.17947801).

Code availability

No new code has been developed for this study. The I3ELVIS code can be accessed at https://zenodo.org/records/11486349.

Received: 20 May 2025; Accepted: 8 January 2026;
Published online: 21 January 2026

References

1. Philippon, M. & Corti, G. Obliquity along plate boundaries. *Tectonophysics* **693**, 171–182 (2016).
2. Brune, S., Williams, S. E. & Müller, R. D. Oblique rifting: the rule, not the exception. *Solid Earth* **9**, 1187–1206 (2018).
3. Jeanniot, L. & Buiter, S. J. H. A quantitative analysis of transtensional margin width. *Earth Planet. Sci. Lett.* **491**, 95–108 (2018).
4. Brune, S. Evolution of stress and fault patterns in oblique rift systems: 3-D numerical lithospheric-scale experiments from rift to breakup. *Geochem. Geophys. Geosyst.* **15**, 3392–3415 (2014).
5. Farangitakis, G. P., Heron, P. J., McCaffrey, K. J. W., van Hunen, J. & Kalnins, L. M. The impact of oblique inheritance and changes in relative plate motion on the development of rift-transform systems. *Earth Planet. Sci. Lett.* **541**, 116277 (2020).

6. Beaussier, S., Gerya, T. & Burg, J. P. 3D numerical modelling of the Wilson cycle: structural inheritance of alternating subduction polarity. *Geol. Soc. Spec. Publ.* **470**, 439–461 (2019).
7. Bellahsen, N. et al. Pre-existing oblique transfer zones and transfer/transform relationships in continental margins: new insights from the southeastern Gulf of Aden, Socotra Island, Yemen. *Tectonophysics* **607**, 32–50 (2013).
8. Müller, R. D. et al. A global plate model including lithospheric deformation along major rifts and orogens since the Triassic. *Tectonics* **38**, 1884–1907 (2019).
9. Gerya, T. V. Dynamical instability produces transform faults at mid-ocean ridges. *Science* **329**, 1047–1050 (2010).
10. Lachenbruch, A. H. Dynamics of a passive spreading center. *J. Geophys. Res.* **81**, 1883–1902 (1976).
11. Tuckwell, G., Bull, J. & Sanderson, D. Mechanical control of oceanic plate boundary geometry. *Tectonophysics* **313**, 265–270 (1999).
12. Brune, S. & Autin, J. The rift to break-up evolution of the Gulf of Aden: insights from 3D numerical lithospheric-scale modelling. *Tectonophysics* **607**, 65–79 (2013).
13. Abelson, M. & Agnon, A. Mechanics of oblique spreading and ridge segmentation. *Earth Planet. Sci. Lett.* **148**, 405–421 (1997).
14. Lin, J., Purdy, G., Schouten, H., Sempere, J. & Zervas, C. Evidence from gravity data for focused magmatic accretion along the Mid-Atlantic Ridge. *Nature* **344**, 627–632 (1990).
15. Gregg, P. M., Behn, M. D., Lin, J. & Grove, T. L. Melt generation, crystallization, and extraction beneath segmented oceanic transform faults. *J. Geophys. Res. Solid Earth* **114**, 1–16 (2009).
16. Maia, M. et al. Extreme mantle uplift and exhumation along a transpressive transform fault. *Nat. Geosci.* **9**, 619–623 (2016).
17. Grevemeyer, I., Rüpke, L. H., Morgan, J. P., Iyer, K. & Devey, C. W. Extensional tectonics and two-stage crustal accretion at oceanic transform faults. *Nature* **591**, 402–407 (2021).
18. Püthe, C. & Gerya, T. Dependence of mid-ocean ridge morphology on spreading rate in numerical 3-D models. *Gondwana Res.* **25**, 270–283 (2014).
19. Buck, W. R., Lavier, L. L. & Poliakov, A. N. Modes of faulting at mid-ocean ridges. *Nature* **434**, 719–723 (2005).
20. Brune, S., Popov, A. A. & Sobolev, S. V. Modeling suggests that oblique extension facilitates rifting and continental break-up. *J. Geophys. Res. Solid Earth* **117**, B08402 (2012).
21. Gerya, T. V. Origin and models of oceanic transform faults. *Tectonophysics* **522-523**, 34–54 (2012).
22. Liu, M., Gerya, T. & Rozel, A. B. Self-organization of magma supply controls crustal thickness variation and tectonic pattern along melt-poor mid-ocean ridges. *Earth Planet. Sci. Lett.* **584**, 117482 (2022).
23. Schierjott, J. C., Thielmann, M., Rozel, A. B., Golabek, G. J. & Gerya, T. V. Can grain size reduction initiate transform faults?—Insights from a 3-D numerical study. *Tectonics* **39**, e2019TC005793 (2020).
24. Ammann, N., Liao, J., Gerya, T. & Ball, P. Oblique continental rifting and long transform fault formation based on 3D thermomechanical numerical modeling. *Tectonophysics* **746**, 106–120 (2018).
25. Okino, K., Kasuga, S. & Ohara, Y. A new scenario of the Parece Vela basin genesis. *Mar. Geophys. Res.* **20**, 21–40 (1998).
26. Dick, H. J. B., Lin, J. & Schouten, H. An ultraslow-spreading class of ocean ridge. *Nature* **426**, 405–412 (2003).
27. Ohara, Y., Fujioka, K., Ishii, T. & Yurimoto, H. Peridotites and gabbros from the Parece Vela back-arc basin: Unique tectonic window in an extinct back-arc spreading ridge. *Geochem. Geophys. Geosyst.* **4**, 149–168 (2003).
28. Leroy, S. et al. From rifting to oceanic spreading in the Gulf of Aden: a synthesis. *Arab. J. Geosci.* **5**, 859–901 (2012).
29. Chang, S. J. & Van der Lee, S. Mantle plumes and associated flow beneath Arabia and East Africa. *Earth Planet. Sci. Lett.* **302**, 448–454 (2011).
30. Hey, R. et al. Multibeam investigation of the active North Atlantic plate boundary reorganization tip. *Earth Planet. Sci. Lett.* **435**, 115–123 (2016).
31. Baines, G. et al. Evolution of the Southwest Indian Ridge from 55°45′E to 62°E: Changes in plate-boundary geometry since 26 Ma. *Geochem. Geophys. Geosyst*. **8**, Q06022 (2007).
32. Kokhan, A. V., Dubinin, E. P. & Sushchevskaya, N. M. Structure and evolution of the eastern part of the southwest Indian Ridge. *Geotectonics* **53**, 449–467 (2019).
33. Stubseid, H., Bjerga, A., Pedersen, L.-E. & Pedersen, R. Extreme mantle heterogeneity revealed by geochemical investigation of in situ lavas at the central Mohns Ridge, Arctic Mid-Ocean Ridges. *Geochem. Geophys. Geosyst*. **25**, e2024GC011704 (2024).
34. Seton, M. et al. A global data set of present-day oceanic crustal age and seafloor spreading parameters. *Geochem. Geophys. Geosyst.* **21**, e2020GC009214 (2020).
35. Zhang, T., Gordon, R. G. & Wang, C. Oblique seafloor spreading across intermediate and superfast spreading centers. *Earth Planet. Sci. Lett.* **495**, 146–156 (2018).
36. Brune, S., Williams, S. E., Butterworth, N. P. & Muller, R. D. Abrupt plate accelerations shape rifted continental margins. *Nature* **536**, 201–204 (2016).
37. Gerya, T. V. & Yuen, D. A. Characteristics-based marker-in-cell method with conservative finite-differences schemes for modeling geological flows with strongly variable transport properties. *Phys. Earth Planet. Inter.* **140**, 293–318 (2003).
38. Gerya, T. V. Three-dimensional thermomechanical modeling of oceanic spreading initiation and evolution. *Phys. Earth Planet. Inter.* **214**, 35–52 (2013).
39. Jourdon, A., Kergaravat, C., Duclaux, G. & Huguen, C. Looking beyond kinematics: 3D thermo-mechanical modelling reveals the dynamics of transform margins. *Solid Earth* **12**, 1211–1232 (2021).
40. Crameri, F. et al. A comparison of numerical surface topography calculations in geodynamic modelling: an evaluation of the 'sticky air' method. *Geophys. J. Int.* **189**, 38–54 (2012).
41. Hirth, G. & Kohlstedt, D. L. Rheology of the upper mantle and the mantle wedge: a view from the experimentalists. *Geophys. Monogr. Ser.* **138**, 83–106 (2003).
42. Martinez, F. & Hey, R. Mantle melting, lithospheric strength and transform fault stability: Insights from the North Atlantic. *Earth Planet. Sci. Lett.* **579**, 117351 (2022).
43. Morishige, M. Spatial variations in the degree of upper-mantle depletion in a mid-ocean ridge–Transform fault system. *Geochem. Geophys. Geosyst*. **25**, e2023GC011227 (2024).
44. Katz, R. F., Spiegelman, M. & Langmuir, C. H. A new parameterization of hydrous mantle melting. *Geochem. Geophys. Geosyst.* **4**, 1073 (2003).
45. Schettino, A., Macchiavelli, C., Pierantoni, P. P., Zanoni, D. & Rasul, N. Recent kinematics of the tectonic plates surrounding the Red Sea and Gulf of Aden. *Geophys. J. Int.* **207**, 457–480 (2016).
46. Demets, C., Merkuryev, S. & Sauter, D. High resolution reconstructions of the Southwest Indian Ridge, 52 Ma to present: implications for the breakup and absolute motion of the Africa plate. *Geophys. J. Int.* **226**, 1461–1497 (2021).

Acknowledgements

We appreciate Nicolas Riel and two anonymous reviewers for their valuable comments and suggestions for improving the manuscript. We thank Alireza Bahadori for editorial handling and helpful comments. J.L. acknowledges funding from the National Natural Science Foundation of China (42222406). W.L. acknowledges funding from the National Key R&D Program of China (2023YFF0803204). S.B. has been funded by the European Union (ERC, EMERGE, 101087245). We thank Dr. Jiarong Qing, Linfeng Liao for their constructive suggestions on this work. Numerical simulations were run on the clusters of the National Supercomputer Center in Guangzhou (Tianhe-II)

and the supercomputing system in the Supercomputing Center of the University of Science and Technology of China.

Author contributions

H.S., J.L., and W.L. conceived the initial idea and model. T.G. provided the numerical code and improved the study design. H.S. performed numerical experiments. H.S., W.L., J.L., S.B., and T.G. participated in result interpretation and paper preparation.

Competing interests

The authors declare no competing interests.

Additional information

Supplementary information The online version contains supplementary material available at https://doi.org/10.1038/s43247-026-03201-y.

Correspondence and requests for materials should be addressed to Jie Liao or Wei Leng.

Peer review information *Communications Earth and Environment* thanks Nicolas Riel and the other anonymous reviewer(s) for their contribution to the peer review of this work. Primary handling editor: Alireza Bahadori. A peer review file is available.